NANO · MICRO small
www.small-journal.com

Battery-Free, Wireless, Ionic Liquid Sensor Arrays to Monitor Pressure and Temperature of Patients in Bed and Wheelchair

*Hyeonseok Han, Yong Suk Oh, Seokjoo Cho, Hyunwoo Park, Sung-Uk Lee, Kabseok Ko, Jae-Man Park, Jungrak Choi, Ji-Hwan Ha, Chankyu Han, Zichen Zhao, Zhuangjian Liu, Zhaoqian Xie, Je-Sang Lee, Weon Gi Min, Byeong-Ju Lee, Jahyun Koo, Dong Yun Choi, Minkyu Je, Jeong-Yun Sun, and Inkyu Park**

Repositioning is a common guideline for the prevention of pressure injuries of bedridden or wheelchair patients. However, frequent repositioning could deteriorate the quality of patient's life and induce secondary injuries. This paper introduces a method for continuous multi-site monitoring of pressure and temperature distribution from strategically deployed sensor arrays at skin interfaces via battery-free, wireless ionic liquid pressure sensors. The wirelessly delivered power enables stable operation of the ionic liquid pressure sensor, which shows enhanced sensitivity, negligible hysteresis, high linearity and cyclic stability over relevant pressure range. The experimental investigations of the wireless devices, verified by numerical simulation of the key responses, support capabilities for real-time, continuous, long-term monitoring of the pressure and temperature distribution from multiple sensor arrays. Clinical trials on two hemiplegic patients confined on bed or wheelchair integrated with the system demonstrate the feasibility of sensor arrays for a decrease in pressure and temperature distribution under minimal repositioning.

1. Introduction

Pressure injuries are a wound caused by prolonged pressure on skin and underlying tissue over bony prominences, deteriorated by an increase in local skin temperature. In particular, these injuries, accompanied by severe pain, loss of function and complex complications, pose a high risk for bedridden or wheelchair patients.[1,2] The development of pressure injuries has a significant impact on patient in terms of worsened quality of life, psychological trauma and extended hospital stays, along with increased economic burdens for medical treatment.[3–5] For the prevention of pressure injuries, clinical practice guidelines, recommended by the National Pressure Injury Advisory

---

H. Han, S. Cho, J. Choi, J.-H. Ha, C. Han, I. Park
Department of Mechanical Engineering
Korea Advanced Institute of Science and Technology
Daejeon 34141, Republic of Korea
E-mail: inkyu@kaist.ac.kr

Y. S. Oh
Department of Mechanical Engineering
Changwon National University
Changwon 51140, Republic of Korea

H. Park, M. Je
School of Electrical Engineering
Korea Advanced Institute of Science and Technology
Daejeon 34141, Republic of Korea

S.-U. Lee
Advanced 3D Printing Technology Development Division
Korea Atomic Energy Research Institute
Daejeon 34057, Republic of Korea

K. Ko
Department of Electronics Engineering
Kangwon National University
Chuncheon 24341, Republic of Korea

The ORCID identification number(s) for the author(s) of this article can be found under https://doi.org/10.1002/smll.202205048.

DOI: 10.1002/smll.202205048

J.-M. Park, J.-Y. Sun
Department of Materials Science & Engineering
Seoul National University
Seoul 08826, Republic of Korea

Z. Zhao, Z. Xie
State Key Laboratory of Structural Analysis for Industrial Equipment
Dalian University of Technology
Dalian 116024, P. R. China

Z. Liu
Institute of High-Performance Computing
Agency for Science
Technology and Research
Singapore 138632, Singapore

J.-S. Lee
Department of Rehabilitation Medicine
Gimhae Hansol Rehabilitation & Convalescent Hospital
Gimhae 50924, Republic of Korea

W. G. Min
Department of Planning and Development
Gimhae Hansol Rehabilitation & Convalescent Hospital
Gimhae 50924, Republic of Korea

B.-J. Lee
Department of Rehabilitation Medicine
Pusan National University Hospital
Busan 49241, Republic of Korea

Panel (NPIAP), involve repositioning at regular intervals for patients confined in clinical bed or wheelchair.[6] However, an appropriate guideline for the repositioning, typically every 2 h, can depend on not only types of mattresses, including air pockets, memory foams and pocket spring, but also critical locations of skin prone to developing pressure injuries. In addition, frequent repositioning leads to decreasing the quality of sleep in patients, interfering with physical activities of patients, and increasing a high risk for back pain or musculoskeletal injuries for patients or caregivers.

Recent advances in technologies of wireless platform offer physiological signals for prevention, diagnosis, and treatment of diseases at early stage. In particular, the wireless platforms with multimodal sensors, including Near Field Communication (NFC) or Bluetooth Low Energy (BLE) platforms, have great potential for continuous monitoring of pressure and temperature at interfaces between the skin and various media, including bed mattresses,[7,8] prosthetic sockets[9] and therapeutic compression garments.[10] However, it is challenging to continuously measure pressures with high accuracy and reliability on locations of interest due to a mismatch between the effective area of body weight and the interfacial area of the single sensor. A few reports suggest several pressure sensor arrays for measurement of pressure distribution at locations of interest.[11–14] Integration of this sensor array with the Bluetooth Low Energy (BLE) platform needs a large number of bulky batteries for long-term monitoring, which pose a risk for developing secondary injuries at skin interfaces.[15] In this context, multiple sensors integrated with the NFC platforms and systems can support capabilities for continuous monitoring of pressure distribution at skin interfaces over full body coverage for long term monitoring without bulky batteries.[7,8]

Previous studies have introduced pressure sensors based on various mechanisms such as piezoresistive,[16–18] capacitive,[19–21] piezoelectric,[22,23] and triboelectric effects.[24,25] In particular, piezoresistive pressure sensors using metal film, CNT, graphene, ionic liquid, and liquid metal have great potential for integrating the wireless platforms owing to simple device design and readout circuit. For real clinical applications, the pressure sensor should have a thin, soft form factor for conformal, irritation-free contact to skin, excellent sensitivity, negligible hysteresis, high linearity and cyclic stability over required pressure range.[7,8] Furthermore, by collecting the pressure sensors in proximity to one another or using the pressure sensor arrays, capabilities for accurate, reliable and continuous measurement of pressure distribution can provide a quantitative basis for the guideline of appropriate repositioning to resolve the issues associated with the mismatch in effective area. In addition, spatial temperature distribution measured on the skin surface can serve as one of additional indicators related to the skin breakdown arising from an increase in tissue metabolism and oxygen consumption using time-integrated and statistical analysis.[26–28]

As an advanced sensor and system for previously reported technologies,[7,8] this paper introduces a method for continuous multi-site monitoring of pressure and temperature distribution from a strategically deployed sensor array at critical skin interfaces via a battery-free, wireless ionic liquid pressure sensor. The pressure sensor based on an internal flow of ionic liquid filled inside a roof collapsed microchannel shows excellent sensitivity as well as negligible hysteresis, high linearity, and cyclic stability over relevant pressure range. The characteristics of the sensor integrated with the NFC platform, verified by experimental measurement and numerical simulation, present technical foundations. In addition, the strategic deployment of the wireless, multiple devices in proximity to one another mounted at different locations of curved skin provides continuous, quantitative information for simultaneously capturing pressure and temperature distribution under change in posture. Clinical trials on two hemiplegic patients demonstrate the feasibility and reliability of the sensor arrays for decreasing local pressures and temperatures of a patient under minimal repositioning confined to a bed or wheelchair integrated with the battery-free, wireless system.

2. Results

2.1. Materials, Device, and Mechanism

Figure 1a presents an exploded view schematic illustration of a battery-free, wireless sensing platform that includes a near-field communication system-on-a-chip (NFC SoC), a receiver coil (antenna), a negative temperature coefficient (NTC; NTCG-064EF104FTBX, TDK Corporation, Japan) thermistor as a temperature sensor, and a pressure sensor on a flexible printed circuit board (fPCB). The pressure sensor has an ionic liquid (1-ethyl-3-methylimidazolium ethyl sulfate; [EMIM][EtSO4]) inside a polydimethylsiloxane (PDMS) microfluidic layer that consists of a microchannel and a reservoir (Figure S1, Supporting Information). The fPCB formed by patterning layers of copper (Cu) and a polyimide (PI) (PI/Cu/PI/Cu/PI, 28/22/13/22/28 μm in thickness) serves as a substrate for the electronic components, pressure sensor and temperature sensor. Figure S2, Supporting Information, shows a schematic illustration of power delivery from a primary antenna connected to an NFC reader to the receiver antenna of the wireless sensing platform via a resonant magnetic inductive coupling. The quality factor (Q) of the wireless sensing platform is a design consideration for evaluating data communication quality. The Q value of the platform at a resonant frequency of 13.56 MHz is 19.36 as measured with a vector network analyzer

---

J. Koo
School of Biomedical Engineering
Korea University
Seoul 02841, Republic of Korea
J. Koo
Interdisciplinary Program in Precision Public Health
Korea University
Seoul 02841, Republic of Korea
D. Y. Choi
Biomedical Manufacturing Technology Center
Korea Institute of Industrial Technology (KITECH)
Yeongcheon 38822, Republic of Korea
J.-Y. Sun
Research Institute of Advanced Materials (RIAM)
Seoul National University
Seoul 08826, Republic of Korea

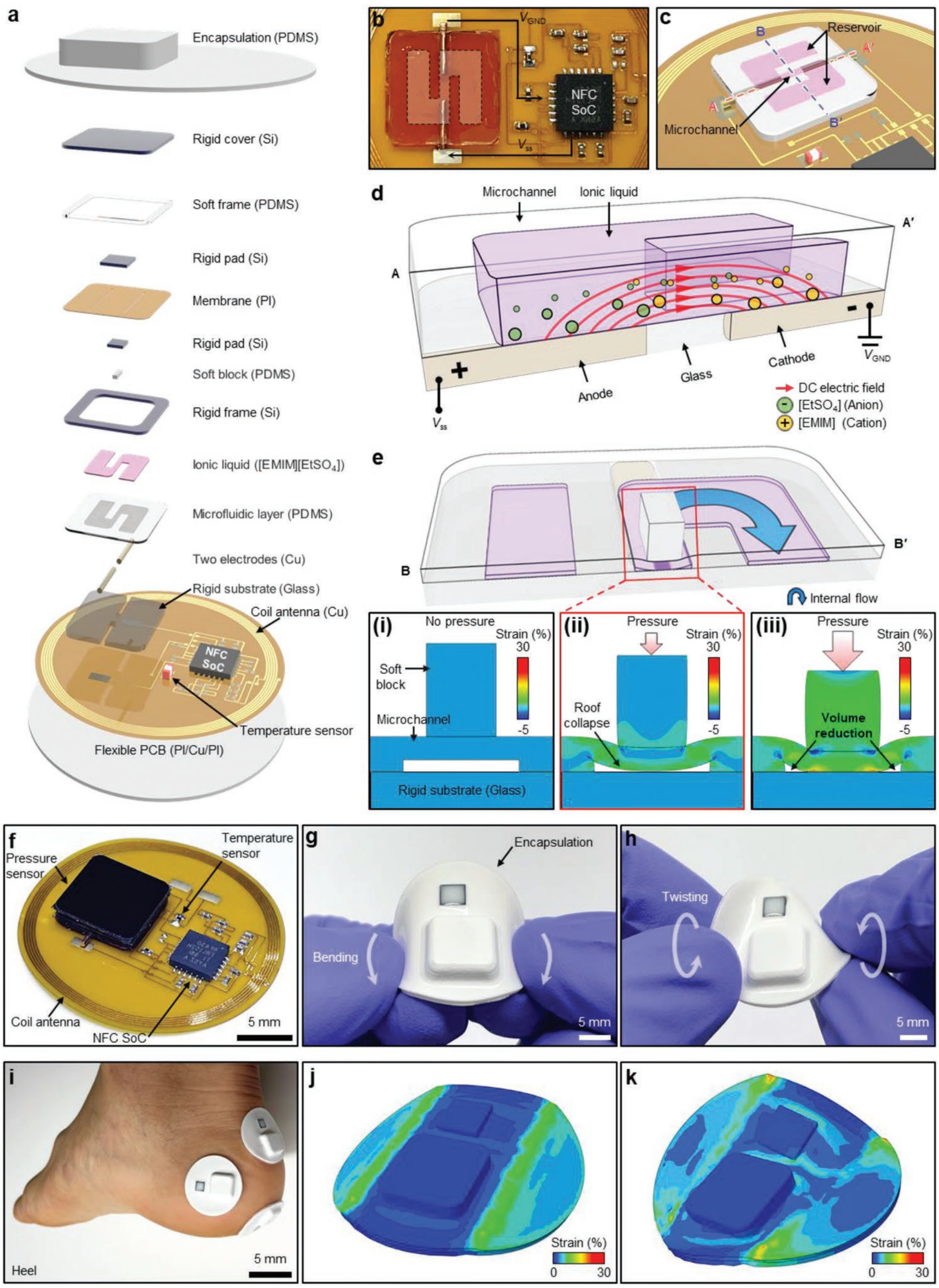

Figure 1. Schematic illustrations and images for a battery-free, wireless pressure sensing device and mechanism. a) Exploded view of the battery-free, wireless, and ionic liquid pressure sensor. b) Photograph of NFC SoC supplying V_{ss} connected to the anode and V_{GND} connected to the cathode. c) Isometric view of a microfluidic layer filled with an ionic liquid. d) Cross-sectional view of the microfluidic layer that includes ion transport due to DC power supplied by the wirelessly delivered power. e) Cross-sectional view of the microfluidic layer to describe the working principle. Insets show sequential FEA results of microchannel: i) no pressure; ii) roof collapse of microchannel with low pressure; and iii) a further volume reduction of microchannel under high pressure. Photograph of a device f) before and g) after packaging in a bent configuration and h) in a twisted configuration. i) Photograph of the multiple devices attached to the curved skin. FEA results of the device in a j) bending and k) twisting configurations.

(VNA; TTR503A, Tektronix, USA) in Figure S3a, Supporting Information, comparable with commercial coils operating at Q values between 10 to 30 (Figure S3b, Supporting Information).[29] VNA measured S-parameters between the primary antenna and the coil antenna to calculate the power transfer efficiency (PTE; η) of 74.6 ± 1.9% ($n = 5$) (Note S1 and Figure S3c, Supporting Information). The ionic liquid pressure sensor and the temperature sensor are connected with two voltage dividers to convert their changes in resistance to voltage outputs. The two voltage signals feed two analog-to-digital converters (ADCs) of NFC SoC that convert the analog voltage signals into the digital signals, which are wirelessly recorded and logged in a data storage format according to ISO 15693 protocol at 13.56 MHz.

Figure 1b,c presents a photograph and an isometric view of the microfluidic layer filled with an ionic liquid over a rigid substrate (glass) with two Cu electrodes mounted on the fPCB, electrically connected to the NFC SoC that supports V_{ss} to an anode and V_{GND} to a cathode. Figure 1d shows a cross-sectional schematic illustration (A–A′) of the ionic liquid-filled microfluidic layer to describe the working principle of an ion transport. The wirelessly delivered power allows the NFC SoC to supply a direct current (DC) voltage of 1.5 V at two electrodes, generating a DC electric field to the ionic liquid-filled microfluidic layer for ion transport. This approach eliminates the need for a battery and its associated bulk and weight for operation of the ionic liquid pressure sensor. The DC electric field separates anions ([EtSO4]) toward the anode and cations ([EMIM]) toward the cathode (Figure S4 and Note S2, Supporting Information). Figure 1e shows a cross-sectional schematic illustration (B–B′) of the ionic liquid-filled microfluidic layer to describe the working principle for an internal flow of ionic liquid between the reservoir and the microchannel under loading. The pressure applied at the soft block (PDMS, $1 \times 0.5 \times 0.4$ mm^3) generates the internal flow of ionic liquid from the microchannel ($5 \times 0.5 \times 0.05$ mm^3) with a roof thickness of 100 μm toward the reservoir ($5 \times 1.5 \times 0.05$ mm^3). The internal flow facilitates a substantial reduction in the cross-sectional area of the microchannel, which can increase a fractional change in resistance of the microchannel under an applied pressure, as shown in Figure 1e(ii,iii). Video S1, Supporting Information, shows a top view of the microchannel deformation below the soft block under the pressure. In addition, a total resistance of the microfluidic layer includes two large charge transfer resistance (R_{ct}) at the Cu electrode–ionic liquid interfaces and a microchannel resistance (R_{ch}), as shown in Figure S5 and Note S3, Supporting Information. Since R_{ct} is a high resistance of ≈10 Mohm, the fractional change in the total resistance of ionic liquid pressure sensor increases with the initial value of R_{ch} under an applied pressure. Two following approaches for increasing the initial value of R_{ch} involve: 1) lower aspect ratio (height/width) of the microchannel (Figure S6, Supporting Information); and (2) pre-compression for a volume reduction of the microchannel.

Figure 1f presents a photograph of the battery-free, wireless sensing platform that includes the ionic liquid pressure sensor and the temperature sensor connected to the NFC SoC and the coil antenna on the fPCB. Figure 1g,h shows photographs of the device in bended and twisted configurations. After encapsulation of PDMS, a thin, soft device supports protection of the electronics from mechanical/electrical damage by external stimuli (e.g., stress concentration, excreted biofluid) and conformal, irritation-free interfaces to the skin. This device enables multiple sensors to conformally attach to the skin of curved body parts such as a right heel, as shown in Figure 1i. In addition, Figure 1j,k shows FEA results of a wireless sensing platform, which exhibit a negligible influence by mechanical deformations, including the maximum bending angle of ≈40° and the maximum twisting angle of ≈30°.

2.2. Design Features and Performance Characteristics of Ionic Liquid Pressure Sensor for Battery-Free, Wireless Multiple Devices

Figure 2a presents a cross-sectional schematic illustration of an assembled pressure sensor with the pre-compression that meets the requirements, including high sensitivity, accurate responses with negligible hysteresis, insensitivity to bending and shear forces, over a relevant pressure range for these applications. The "Experimental section" provides a detailed process for fabricating the pressure sensor with dimensional information. In Figure 2a, the assembled pressure sensor includes two key components as follows: 1) the soft block for pre-compression without external load (Figure S7d–g, Supporting Information) and 2) the soft frame for adjusting the sensitivity (Figure S7f, Supporting Information). In order to secure the uniformity of the pressure sensor, a universal testing machine (UTM; AGS-X, Shimadzu, Japan) with a high-level control resolution of 0.025 μm at a speed of 0.5 μm min^{-1} compressed the epoxy bonding with a constant load during assembly process as shown in Figure S8, Supporting Information. Evaluation of the response of the ionic liquid pressure sensor without upper components against applied pressure to the soft block preceded assembly of the pressure sensor in advance (Figure S9a, Supporting Information). The pre-compressed soft block leads to a volume reduction in the microchannel below the soft block under loading, resulting in significantly increasing the fractional change in resistance, as described in Figure 2b. The soft frame tunes the sensitivity of the pressure sensor based on the compressive modulus of various elastomers, including Dragon Skin (E = 100 kPa) and PDMS (E = 2.5 MPa). The rigid frame and rigid pad enable a robustness of pressure sensor due to a decrease of stress at interfaces of the soft frame under shear loadings.[7] Figure 2b compares the responses of the ionic liquid pressure sensor without upper components under loading at different pre-compression within a pressure range 0–30 kPa. The ionic liquid pressure sensor without upper components exhibits very low sensitivity (0.0006 kPa^{-1}) without the pre-compression due to a large charge transfer resistance (R_{ct}) on the order of ≈10 Mohm at the Cu electrode–ionic liquid interfaces compared to a microchannel resistance (R_{ch}) as presented in Figure S5 and Note S3, Supporting Information. On the other hand, the ionic liquid pressure sensor with the pre-compression exhibits enhanced sensitivities of 0.0015, 0.0100 and 0.0182 kPa^{-1} depending on compressed pressure of 50, 100 and 150 kPa owing to an increase of the initial R_{ch}. These results indicate that the ionic liquid pressure sensor can provide more than 10 times improvement of the fractional change in resistance compared to that obtained using a typical microchannel without pre-compression. Furthermore, applying pressure in addition to the pre-compression of 180 kPa to the ionic liquid pressure sensor without upper components exhibits a high sensitivity of 0.68 kPa^{-1} due to significant volume reduction of microchannel through pre-compression (Figure S9b, Supporting Information). To our best knowledge, among microchannel integrated pressure sensors filled with conductive liquid, the ionic liquid pressure sensor without upper components exhibits the highest sensitivity (kPa^{-1}) as well as small form factor (mm^3), an important consideration for wearable devices, in Table S1, Supporting Information. However, we utilized the ionic liquid

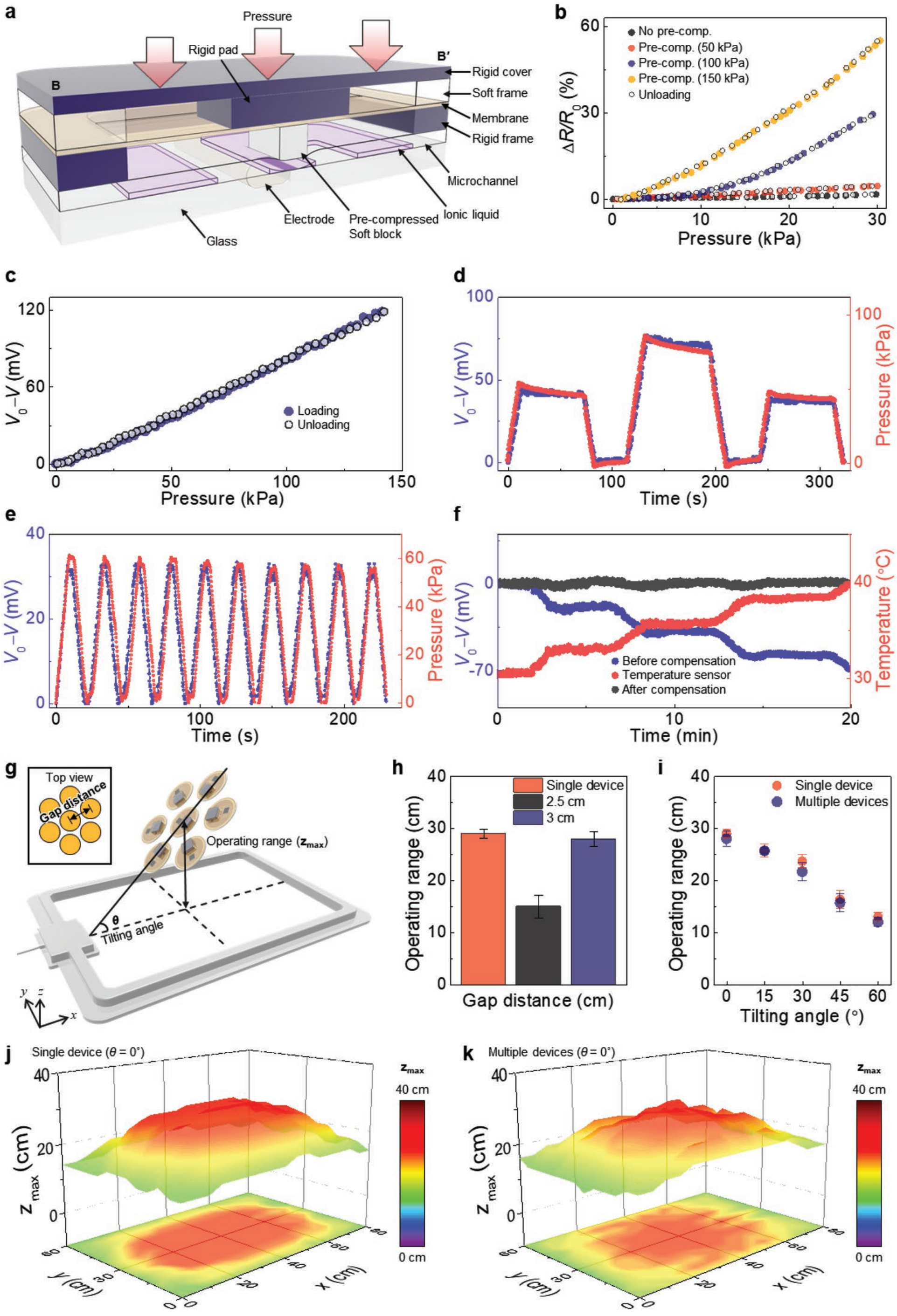

Figure 2. Design features and performance characteristics of ionic liquid pressure sensor for battery-free, wireless multiple devices. a) Cross-sectional schematic illustration of the ionic liquid pressure sensor to pre-compress soft block and operating mechanism of the pressure sensor. b) Fractional change in resistance of the ionic liquid pressure sensor according to pre-compression of the microchannel. c) Response of the wireless pressure sensor under pressure loading and unloading. d) Change of the ADC values measured from the wireless pressure sensor under constant loadings of 75, 150, and 75 kPa, respectively. e) Change of the ADC values measured from the wireless pressure sensor during 10 cycles of loading/unloading. f) Change of the ADC values measured from the wireless pressure sensor when temperature increases and its compensated ADC values. g) Schematic illustration of experimental setup for comparison of operating range of multiple devices depending on h) the gap distance between wireless devices and i) the tilting angle of multiple device. Comparison of operating range for j) single device and k) multiple devices at tilting angle of 0° from primary antenna ($62 \times 83.8 \times 2.6$ cm^3).

pressure sensor with sensitivity of less than 0.0182 kPa^{-1} for better reproducibility (i.e., sensor-to-sensor variation). Figure S10, Supporting Information, presents the fractional change in resistance of the ionic liquid pressure sensor without and with reservoir. The ionic liquid pressure sensor with a reservoir shows a relatively stable linear response over a relevant pressure range due to the internal flow under loading and unloading compared to that obtained without using a reservoir.

Figure S11a–f, Supporting Information, present experimental results of the pressure sensor that satisfy the operating range of 0–100 kPa required for the prevention of pressure injuries for both bedridden or wheelchair-bound patient.[30,31] Figure S11a, Supporting Information, shows responses of the pressure sensor to a cycle of loading and unloading without and with a soft frame (E = 100 kPa for Dragon Skin and E = 2.5 MPa for PDMS). The pressure sensor shows a high linearity ($R^2 > 0.99$), negligible hysteresis within the fractional change in resistance ($\Delta R/R$) of 10%. The pressure sensor provides capabilities for tuning the sensitivity over the operation range of pressure using different types of soft frame. Figure S11b, Supporting Information, indicates the fractional change in resistance of the pressure sensor with negligible drift (<0.1%) under 3 repeated loadings of 35, 85 and 35 kPa. In Figure S11c, Supporting Information, the pressure sensor shows a stable response against more than 1000 repeated loading of 50 kPa with a negligible drift as well as the cyclic durability of the sensor. Figure S11d, Supporting Information, presents the response of the pressure sensor to temperature ranged from 30 to 40 °C measured by the temperature sensor (NTC). The electrical conductivity of ionic liquid raises with increasing temperature due to a reduction in the viscosity of the ionic liquid.[32,33] The resistance of ionic liquid can be compensated using the following equation, $(\Delta R/R)_c = (\Delta R/R)_m + a\Delta T$, where $(\Delta R/R)_c$ is a compensated value and $(\Delta R/R)_m$ is a measured value and a is a calibration factor of 1.12 K^{-1}. The compensated data (black) of the pressure sensor is insensitive to the temperature variation. In addition, the measurement of skin temperature distribution at mounting locations of device can provide medical data for the tissue metabolism and oxygen consumption,[34] as one of ulcer-related variables for assessing the risk of accelerating pressure injuries. Figure S11e, Supporting Information, presents the rapid response time of the pressure sensor under dynamic loading of 40 kPa by showing a negligible delay between response time and load time. Figure S11f, Supporting Information, shows the stable response of the pressure sensor without drift at static load of 35 kPa for more than 30 min.

Figure S12a, Supporting Information, illustrates an experimental setup for evaluating the ionic liquid pressure sensor integrated with a battery-free, wireless platform under a cycle of loading and unloading. The setup consists of a UTM to measure applied pressures, a primary antenna connected to the NFC reader, and a laptop computer for real-time data collection. A stacked wood frame makes a distance from a metal surface of the UTM to support a stable power delivery and data communication with the sensing platform. This setup provides continuous, real-time monitoring for the force–distance data measured from UTM and the voltages obtained from the ADCs of NFC SoC in response to the pressure and temperature at the same time. Figure S12b, Supporting Information, presents a block diagram for the operation of battery-free, wireless sensing system that includes three subsystems: 1) the wireless, battery-free sensing device that converts analog signals of pressure and temperature sensors to digital signals using two voltage dividers and ADC of NFC SoC; 2) the NFC reader connected to the primary antenna that supports power delivery and data communication with the wireless device using the NFC protocols; and 3) the post-processing and real-time monitoring of measured signals using a graphical user interface (GUI) of the computer.

Equivalent circuit diagram (Figure S13, Supporting Information) describes a calibration procedure for the data collected from the wireless device using Equation (1):

$$V_{\text{out}} = \frac{V_{\text{in}} \times R_0}{R_{\text{sens}} + R_0} \tag{1}$$

where V_{out} is an output voltage between 0 and 0.9 V, V_{in} is an input voltage of 1.5 V, R_{sens} is the sensor resistance and R_0 is a reference resistance for voltage tuning, respectively. The values of R_0 are a half the magnitude of the initial resistance for the pressure sensor and 49.9 kΩ for the temperature sensor (NTC). Figure 2c presents the change in the ADC value under a cycle of loading and unloading. The result shows a high sensitivity, negligible hysteresis, negligible drift (<0.5%), high linearity ($R^2 > 0.99$), and high signal-to-noise ratio (SNR) of 206.7 over a wide pressure range of 100 kPa using Equation (2):

$$\text{SNR} = \frac{\Delta V_{\text{signal}}}{\sigma_{\text{noise}}} \tag{2}$$

where ΔV_{signal} is the average signal in measured voltages and σ_{noise} is the standard deviation of the baseline (Figure S14, Supporting Information). Figure 2d presents the change in the ADC value under sequential, constant loadings of 50, 80 and 45 kPa, respectively. Figure 2e shows the response of the pressure sensor against 10 repeated loadings of 60 kPa. Figure 2f presents temperature-compensated ADC values (black) using ADC values (blue and red, respectively) measured from the pressure sensor and the temperature sensor (NTC) under the temperature range of 30–40 °C. The response of pressure sensor decreases from 0 to −70 mV with increasing the temperature. The temperature dependence of ADC value of the pressure sensor can be compensated using the following equation, $(\Delta V)_c = (\Delta V)_m + \beta\Delta T$, where $(\Delta V)_c$ is a compensated value and $(\Delta V)_m$ is a measured value, and β is a calibration factor of 8.9 mV K^{-1}. The compensated ADC values exhibit a standard deviation of ±1.3 mV with a small drift of ≈1.1%, which can provide the appropriate compensation for ΔT of 10 °C.[34,35] Figure S15, Supporting Information, presents the response of the pressure sensors with different thicknesses at the interface between ischium and mattress under a loading of ≈30 kPa. Although the thickness of the pressure sensor increases from 1.95 to 3 mm by bonding additional rigid covers (silicon; 8 × 8 × 0.25 mm^3), the response and standard deviation of the pressure sensor does not change significantly at the interface. Figure 2g presents a schematic illustration of experimental setup for measuring the maximum operating vertical distance ($z_{\max}$) of multiple wireless devices using a Cartesian coordinate system (xyz axis) and a tilting angle (θ) with the origin at the

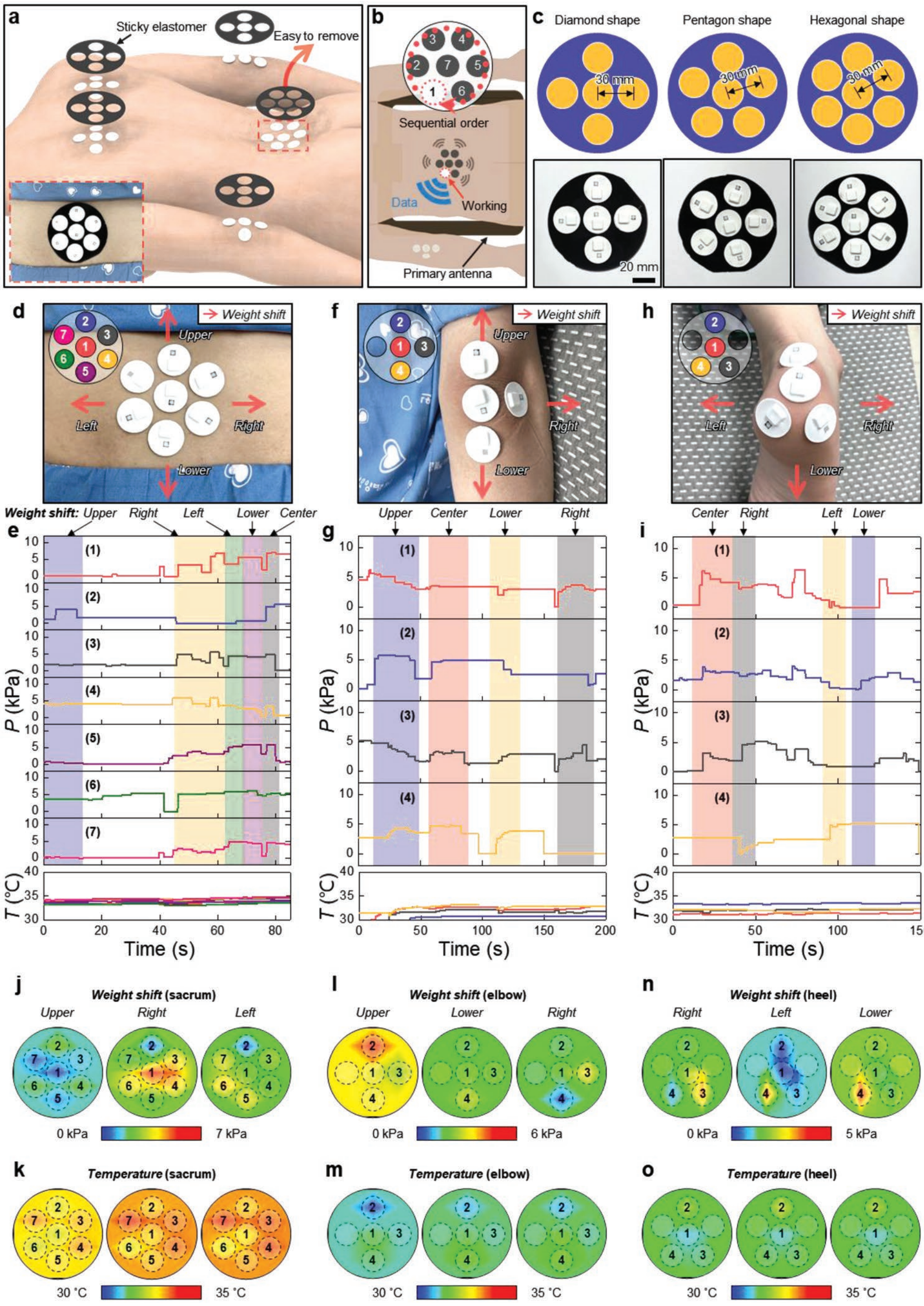

Figure 3. Continuous monitoring and mapping of pressure and temperature distribution using strategically deployed sensor arrays. a) Schematic illustration of a method for strategical deployment of wireless devices at regular distances using a sticky elastomer. Inset shows photograph of the sensor array on 7 holes of the sticky elastomer. b) Schematic illustration of continuous capturing of pressures and temperatures from sensor array in the sequential RF readout scheme through NFC protocol. c) Schematic illustrations and photographs of the strategically deployed wireless devices in proximity to one another with a center-to-center distance of 30 mm, which includes a diamond-shaped array of 5 devices, pentagon-shaped array of 6 devices and hexagon-shaped array of 7 devices. Results of continuous monitoring and mapping of pressure and temperature distribution using the sensor array mounted at d,e) sacrum, f,g) elbow, and h,i) heel. Color map of pressure and temperature distribution using the sensor array mounted at j,k) sacrum, l,m) elbow, and n,o) heel.

left bottom corner of the primary antenna (62 × 83.8 × 2.6 cm^3). Inset shows a gap distance between the centers of each device. Figure 2h compares the $z_{\max}$ of 7 devices at two different gap distances of 2.5 and 3 cm at θ of 0°. The 7 devices with the gap distance of 3 cm shows the $z_{\max}$ of 28 ± 1.41 cm, which is similar to that of 29 ± 0.82 cm obtained using the single device. However, the operation range of 7 devices decreases to 15 ± 2.16 cm with the change of gap distance from 3 to 2.5 cm.

A reduction in the $z_{\max}$ depends on a cross-coupling between adjacent receiver coils of the wireless devices, which leads to not only detuning the resonant frequency of each receiver coil, but also hindering the power transfer from the primary antenna to the receiver coil.[36] Figure S16, Supporting Information, shows the simulation results for the normalized voltages of 7 devices at each location and their average voltages with the gap distance of 2.5 and 3 cm, which indicates the effect of cross-coupling on adjacent receiver coils of the wireless devices (see Note S5, Supporting Information). The modified device design that includes a serpentine trace between the receiver coil and sensor can provide improvement of spatial resolution by about 1 cm in terms of a sensor-to-sensor distance, as shown in Figure S17c, Supporting Information. Figure 2i compares the $z_{\max}$ of 7 devices with a gap distance of 3 cm at different tilting angles. The $z_{\max}$ decreases from 28 ± 1.41 to 12 ± 0.81 cm by increasing the tilting angle from 0° to 60° due to a reduction of magnetic flux passing through the receiver coil. These results indicate that the multiple devices can enable stable operation below $z_{\max}$ of 12 cm and until a tilting angle of 60° over the primary antenna. Figure 2j,k presents the $z_{\max}$ distribution for single device and multiple devices over the entire area of primary antenna, respectively. The multiple devices exhibit stable operation over the $z_{\max}$ distribution of 12–30 cm, which is similar to that of 14–30 cm obtained using a single sensor to cover the entire area in the *xy* plane.

2.3. Strategically Deployed Wireless Sensor Array for Continuous Monitoring and Mapping

Figure 3a presents a schematic illustration of a method for strategical deployment of wireless devices at regular distances using a sticky elastomer with customized cuttings by punches or laser. Inset shows a photograph of the sensor array on 7 holes of the sticky elastomer. This sensor array provides continuous monitoring of pressure and temperature distribution along with the required number of devices, the distance between the devices, and the arrangement of the device at locations of interest in a sequential RF readout scheme, as shown in Figure 3b. The numbers marked on the sensor array indicate the order of operation in a wireless, battery-free mode through NFC protocol. Figure 3c provides schematic illustrations and photographs of the strategically deployed wireless devices in proximity to one another with a center-to-center distance of 30 mm, which includes a diamond-shaped array of 5 devices, pentagon-shaped array of 6 devices, and hexagon-shaped array of 7 devices. The number, distance and arrangement of the sensor array depend on the skin curvature, degree of bony protrusion and area of the locations, including elbow, sacrum, knee and heel. These approaches not only enable individual, specific deployment through repeated clinical trials and accumulated data, but also provide the potential for resolving the aforementioned issues related to the limited resolution of a single sensor, discrepancy of the sensing area and inaccurate measurement. In addition, the wireless device combined with an open layout (e.g., holey structures) supports water evaporation released through sweating, which is helpful for long-term monitoring in Figure S18, Supporting Information.

Feasibility trials involve continuous monitoring of pressure and temperature distribution from the sensor array mounted at a skin interface of an able-bodied subject (male, 38-year-old; height, 178 cm; mass, 85 kg; skin temperature, ≈35 °C) lying in a clinical bed. Figure 3d,e presents a photograph of the hexagon-shaped array of 7 sensors mounted at a sacrum and continuously collected data under change in posture. The sensor array enables continuous capturing of pressure and temperature distribution at the sacrum and its change associated with sequential weight shifting in the upper, right, left, lower, and center directions. The maximum values of pressure at the sacrum are 4.3, 7.0, 5.9, 5.8, and 7.1 kPa in each weight shifting. The temperatures at the sacrum are in the range of 33.0–34.9 °C and their average is 33.9 °C. Figure 3f,g presents a photograph of the T-shaped array of 4 sensors mounted at a left elbow and continuously collected data under change in posture. The sensor array enables continuous capturing of pressure and temperature distribution at the left elbow and its change associated with sequential weight shifting in the right, center, left, and lower directions. The maximum values of pressure at the left elbow are 5.7, 3.6, 4.9, and 4.5 kPa in each weight shifting. The temperatures at the left elbow are in the range of 29.2–33.2 °C and their average is 31.9 °C. Figure 3h,i presents a photograph of Y-shaped array of 4 sensors mounted at a left heel and continuously collected data under change in posture. The sensor array enables continuous capturing of pressure distribution at the left heel and its change associated with sequential weight shifting in the center, right, left, and upper directions. The maximum values of pressure at the left heel are 5.8, 5.1, 5.0, and 5.2 kPa in each weight shifting. The temperatures at the left heel are in the range of 31.1–33.6 °C and their average is 32.2 °C. In addition, Figure S19, Supporting Information, shows a photograph of a hexagonal array of 6 sensors mounted at a right knee in a prone position and continuously collected data under change in posture. The sensor array enables continuous capturing of pressure distribution at the right knee and its change associated with sequential weight shifting in a clockwise direction (center, upper right, and left directions). The maximum values of pressure at the right knee are 5.1, 4.8, 4.7, and 4.8 kPa in each weight shifting. The temperatures at the left heel are in the range of 30.2–32.9 °C and their average is 31.2 °C.

Figure 3j–o presents color maps of the pressure and temperature at different mounting locations of the sensor array, including sacrum, elbow and heel using the time-integrated and statistical analysis described in the Experimental section. These approaches provide visualized, critical information of the average and maximum values at each mounting location during a prolonged period of time, which can be useful to assess statistical correlations related to the development of pressure injuries. For convenience, the sensor numbers for each location are abbreviated (e.g., sensor 1 and sensor 2 on the right elbow are abbreviated as right elbow [S1, S2]). Figure 3j,k and Tables S2 and S3, Supporting Information, show the average/maximum values of pressures and the average values/ranges of temperatures measured at the sacrum under the sequential weight shifting to upper, right, and left directions. Figure 3l,m and Tables S2 and S3, Supporting Information, show corresponding values measured at the elbow under the sequential weight

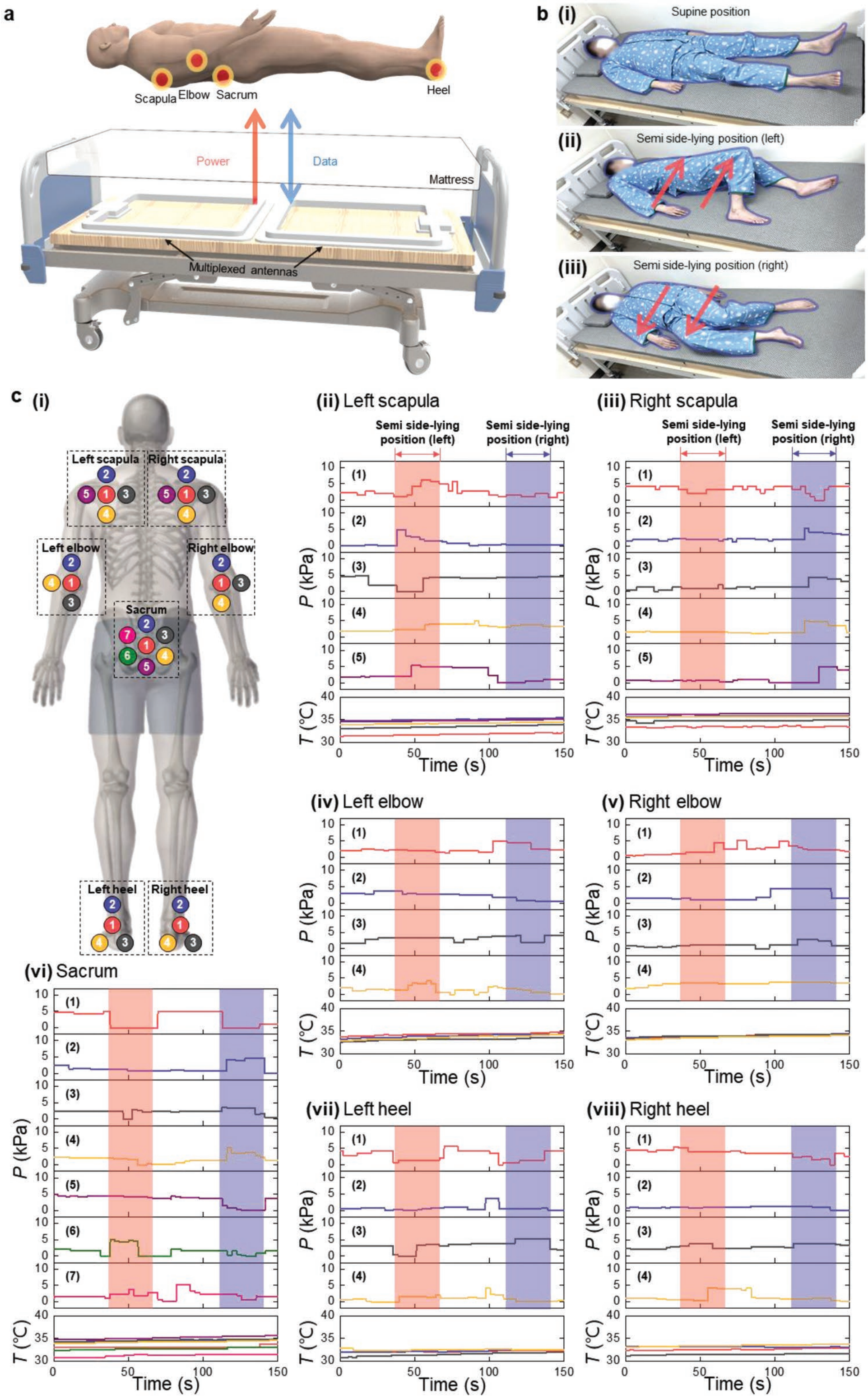

Figure 4. Continuous monitoring and mapping of pressure and temperature distribution at critical sites of a healthy subject (38-year-old male, 85 kg, 175 cm) lying in clinical bed. a) Schematic illustration of battery-free, wireless sensing system integrated with clinical bed for continuous monitoring and mapping of pressure and temperature distribution using sensor arrays mounted at the critical sites of the subject. b) Photographs of the subject lying in clinical bed in a i) supine position, ii) semi side-lying (left) position, and iii) semi side-lying (right) position. c) Results from continuous monitoring of pressure and temperature distribution from the sensor array. i) Schematic illustration of the sensor array mounted at the critical sites of subject, such as ii,iii) scapula, iv,v) elbow, vi) sacrum, and vii,viii) heel.

shifting to upper, lower, and right directions. Figure 3n,o and Tables S2 and S3, Supporting Information, show corresponding values measured at the knee under the sequential weight shifting in the right, left, and lower directions.

2.4. Continuous Multi-Site Monitoring of Pressure and Temperature Distribution under Change in Lying Posture

Figure 4a and Figure S20, Supporting Information, illustrate a battery-free, wireless system integrated with a clinical bed that includes two multiplexed antennas connected to a multiplexer, an NFC reader and a laptop computer for the full-body coverage. Figure S21a, Supporting Information, presents the simulation result of magnetic field distribution of the primary antenna for the clinical bed (see Note S6, Supporting Information). Computational assessments demonstrated that both the specific absorbed radiation (SAR) and the maximum permissible exposure (MPE) follow the guidelines of Federal Communications Commission (FCC) (47 CFR Part 1.1310 and 15).[7,8,37] In addition, elderly patients who participated in the clinical trials under the supervision of medical doctors had no medical problems in our previous study.[7] In Figure 4b, clinical trial involves continuous multi-site monitoring of pressure and temperature distribution for an able-bodied subject (male, 38-year-old; height, 175 cm; mass, 85 kg; skin temperature, ≈35 °C) lying in the clinical bed.

Figure 4b(i–iii) shows photographs of the able-bodied subject in a supine position, a semi side-lying position (left), and a semi side-lying position (right) at different times for sequential weight shifting by himself. The form factor of devices enables conformal contact with skin, without discomfort for the mounting locations of the subject under the postural change.

Figure 4c(i) depicts a schematic anatomical diagram for strategic deployment of the sensor array that include a diamond-shaped array of 5 sensors at both left and right scapula, a T-shaped array of 4 sensors at both left and right elbows, hexagon-shaped array of 7 sensors at a sacrum, and a Y-shaped array of 4 sensors at both left and right heels.

Figure 4c(ii–viii) highlights the results of continuous recordings (sampling rate of 10 Hz) of temperatures and pressures at each sensor array of mounting locations. The temperatures at both scapulae, both elbows, sacrum and both heels are in the range of 31.4–36.5, 32.6–34.8, 30.9–35.7 and 30.9–33.9 °C and their average are 34.6, 33.9, 33.7 and 32.5 °C. The data measured during the left weight shifting in Figure 4c(ii) reveals pressure relief at the right scapula (S1–S3), right elbow (S2), sacrum (S1, S3, S4) and right heel (S1, S3) with increasing pressure at the left scapula (S1–S5), left elbow (S4), sacrum (S6, S7) and left heel (S4). On the other hand, the data collected during the right weight shifting in Figure 4c(iii) exhibit pressure relief at the left scapula (S5), left elbow (S2–S4), sacrum (S1, S5–S7) and left heel (S1, S4) with increasing pressure the right scapula (S2–S5), right elbow (S2, S3), sacrum (S2–S4) and right heel (S3). In addition, Table S4, Supporting Information, shows the average values/ranges of temperature measured at the both scapulae, both elbows, sacrum, and both heels. These data indicate that the strategically deployed sensor arrays can provide a quantitative basis for simultaneous changes in pressures and temperatures at each mounting location of the subject lying in bed during postural changes to a semi side-lying position (left) and a semi side-lying position (right) by himself.

2.5. Continuous Multi-Site Monitoring of Pressure and Temperature Distribution under Change in Sitting Posture

Figure 5a and Figure S22, Supporting Information, show a schematic illustration and a photograph of the battery-free, wireless system integrated with a wheelchair that includes four multiplexed antennas connected to a multiplexer, an NFC reader, and a laptop for full-body coverage. Figure S21b,c, Supporting Information, presents the simulation result of magnetic field distribution of the primary antenna for the wheelchair. Figure 5b shows a photograph of an able-bodied subject (male, 38-year-old; height, 175 cm; mass, 85 kg; skin temperature, ≈35 °C) sitting in wheelchair for continuous multi-site monitoring of pressure and temperature distribution.

Figure 5c depicts a schematic anatomical diagram for the sensor arrays that include a hexagon-shaped array of 7 sensors at a sacrum, a diamond-shaped array of 5 sensors at both left and right ischia, and a Y-shaped array of 4 sensors at both left and right heels. The form factor of devices enables conformal contact with the skin, without discomfort for the mounting locations of the subject sitting in a wheelchair under postural change.

Figure 5d(i–iii) shows photographs of the able-bodied subject sitting in wheelchair and weight shifting motions, including: i) a lateral weight shifting (left); ii) lateral weight shifting (right); and iii) push-up weight shifting for repositioning by himself.

Figure 5e(i–v) highlights results of continuous recordings of pressures and temperature distribution at each sensor array of mounting locations. The data measured during the lateral weight shifting (left) in Figure 5d(i) reveals pressure relief at the right ischium (S1–S5), the left heel (S1) and the right heel (S1, S3) with increasing pressure at the sacrum (S5–S7), the left ischium (S1–S4), the left heel (S4) and the right heel (S4). On the other hand, the data collected during the lateral weight shifting (right) in Figure 5d(ii) exhibits pressure relief at the sacrum (S1, S6–S7), the left ischium (S1–S4), the left heel (S1, S4) and the right heel (S1, S4) with increasing pressure the right sacrum (S3, S4), the left ischium (S5), the right ischium (S1–S5), the left heel (S2, S3) and the right heel (S2, S3). In addition, the data collected during the push-up weight shifting in Figure 5d(iii) exhibits pressure relief at the sacrum (S1, S3–S6), the left ischium (S1–S5), and the right ischium (S1–S5) with increasing pressure to the left heel (S1–S4) and the right heel (S1–S4). In addition, Table S5, Supporting Information, shows the average values/ranges of temperature measured at the sacrum, both ischia, and both heels. These data indicate that the strategically deployed sensor arrays can provide a quantitative basis for simultaneous changes in pressures and temperatures at each mounting location of the subject sitting in a wheelchair against both lateral weight shifting and push-up weight shifting by himself.

2.6. Continuous Multi-Site Monitoring of Pressure and Temperature Distribution Using Cushions for Hemiplegic Patient in Clinical Bed

A minimal repositioning for pressure relief involves rotating the body part or redistributing the weight to other part using

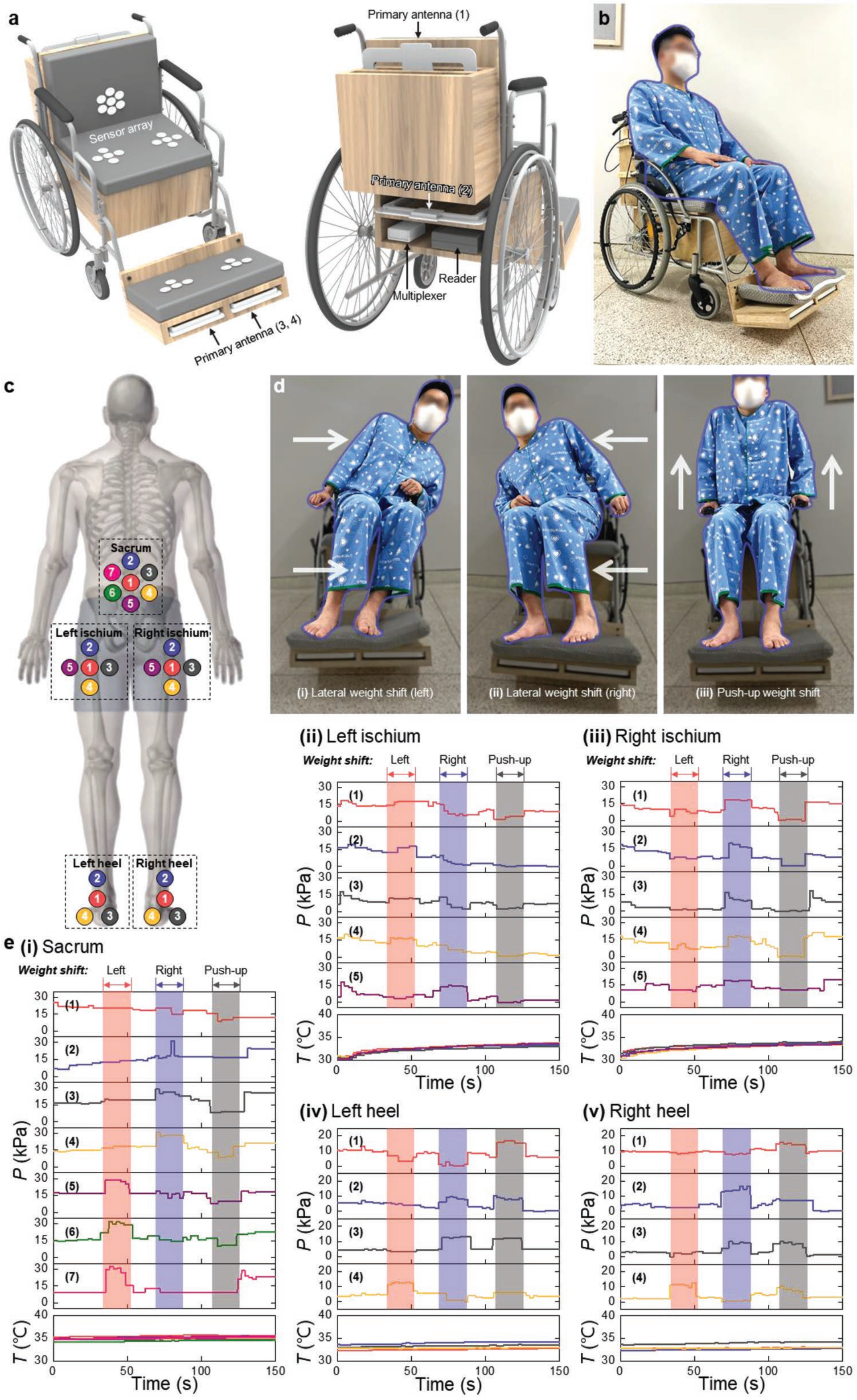

Figure 5. Continuous monitoring and mapping of pressure and temperature distribution at critical sites of a healthy subject (38-year-old male, 85 kg, 175 cm) sitting in wheelchair. a) Schematic illustration of battery-free, wireless sensing system integrated with wheelchair for continuous monitoring of pressure and temperature distribution at the critical sites using sensor arrays. b) Photograph of the subject sitting in the wheelchair. c) Schematic illustration of the sensor array mounted at the critical sites of subject, such as sacrum, ischium and heel. d) Photographs of subject for change in sitting postures, including i) lateral weight shifting (left), ii) lateral weight shifting (right) and iii) push-up weight shifting. e) Results from continuous monitoring of pressure and temperature distribution from the sensor array mounted at the critical sites of subject, including i) sacrum, ii,iii) ischium and iv,v) heel.

a support cushion or a water cushion, as shown in Figure S23, Supporting Information. The minimal repositioning has advantages for not only accurate pressure relief at specific locations, but also prevention of secondary injuries of a patient or a caregiver caused by frequent repositioning. In addition, the water cushion can decrease both local pressure and temperature at critical skins. The sensor arrays mounted at critical multi-sites can support quantitative basis for change in pressure and temperature distribution with minimal repositioning. These approaches are useful for the prevention of pressure injuries for burn patients or patients immobilized for medical treatment.[38]

Continuous multi-site monitoring of pressure and temperature distribution for a hemiplegic patient in a clinical bed demonstrate the feasibility and stability of the strategically deployed sensor array for pressure relief by a support cushion and for lowering local pressures and skin temperatures by a water cushion. One hemiplegic patient is a 62-year-old male patient with left hemiplegia and acromyotonia with medical information as follows: a height of 162 cm, a weight of 73.9 kg, high blood pressure of 125/85 mmHg, albumin of 4.1 g dL^{-1}, and hemoglobin A1c (HbA1c) of 6.2%.

Figure 6a shows photographs of the patient lying in a clinical bed in a supine position with the addition of the support cushion or the water cushion by a caregiver. The support cushion used near a right scapula and a right sacrum in Figure 6a(i,ii) decreases the only local pressures at the skin interfaces, whereas the water cushion near both heels and left sacrum in Figure 6a(iii,iv) lowers both the local pressures and skin temperatures. Figure 6b presents infrared (IR) photographs of the patient with the addition of a water cushion with a temperature of about 20 °C at the skin-mattress interfaces of heels and left sacrum regions. During the clinical trial, the caregiver sequentially placed the support cushion at the right scapula, at the right sacrum, and then the water cushion at the heels, at the left sacrum with 4 min intervals.

Figure 6c(i) illustrates a schematic anatomical diagram of 7 mounting locations of the sensor array, including both scapulae, both elbows, sacrum and both heels of the left hemiplegic patient. Figure 6c(ii–viii) presents continuous multi-site recordings of the temperature and pressure distribution measured from a diamond-shaped array of 5 sensors at the both scapulae, T-shaped array of 4 sensors at the both elbows, hexagon-shaped array of 7 sensors at the sacrum and Y-shaped array of 4 sensors at the both heels, respectively.

Continuous multi-site monitoring of pressure and temperature distribution for a hemiplegic patient in a clinical bed demonstrated the feasibility and stability of the strategically deployed sensor array for pressure relief by a support cushion and for lowering local pressures and skin temperatures by a water cushion. Before describing continuous monitoring data collected from the clinical trial in a clinical bed, color maps that organized the collected data along with a timeline provide readers with an intuitive understanding of the clinical trial in a bed at a glance in Figure S24, Supporting Information. The temperatures (average temperature) are in the range of 31.3–34.0 °C (32.8 °C) at the scapulae, in the range of 31.4–36.1 °C (33.7 °C) at the elbows, in the range of 32.8–34.3 °C (33.6 °C) at the sacrum, and in the range of 30.9–33.5 °C (32.5 °C) at the heels, respectively. Figure 6c(v) depicts the pressure relief at the right scapula (S1, S4, S5) and the right elbow (S1, S2, S4) for 4–8 min by placing the support cushion at right scapula, as shown in Figure 6a(i). Similarly, Figure 6c(vi) shows the pressure relief at the sacrum (S1, S2, S4, S5) between 8 and 12 min by placing the support cushion at right sacrum, as shown in Figure 6a(ii). Table S6, Supporting Information, shows the average values/ranges of temperature measured at the both scapulae, both elbows, sacrum and both heels. For lowering the local skin temperature, the caregiver placed the water cushion of 20 °C under the heels at 12 min, as shown in Figure 6a(i,iii). Figure 6c(vii) shows that the local skin temperature at the left heel (S1–S4) and the right heel (S1–S4) decreases by up to 0.9 (S3) and 2.0 °C (S3). In addition, Figure 6c(vii) shows a reduction in the local skin temperature at the sacrum (S1, S5–S7) up to 1.1 °C (S7) by placing the water cushion under left sacrum, as shown in Figure 6a(ii,iv). At the same time, the sacrum (S1, S2, S5–S7) shows a reduction in pressure by redistributing the weight to other parts due to the water cushion. The maximum values of pressure are 2.6 kPa at the right scapula (S1), 4.9 kPa at the sacrum (S7), 4.5 kPa at the right heel (S1), and 4.3 kPa at the sacrum (S4) for each minimal repositioning using these cushions. Overall, Video S2, Supporting Information, provides continuous multi-site monitoring of pressure and temperature distribution from strategically deployed sensor arrays for bedridden patients through color maps.

Figure S25, Supporting Information, compares pressure–time integral (PTI) values, as a commonly used assessment method for single device and multiple devices for patients lying in clinical bed. The PTI values using the multiple devices show the average, maximum, and minimum values for each critical site at the same time. On the other hand, the PTI values obtained using a single device that depend on mounting locations show minimum values at the left scapula, right elbow and sacrum, while they exhibit maximum values at the right scapula, left elbow, left heel and right heel. These results indicate the PTI values using the multiple devices are useful for an accurate risk assessment caused by lying in a clinical bed.

2.7. Continuous Multi-Site Monitoring of Pressure and Temperature Distribution Using Cushions for Hemiplegic Patient in Wheelchair

Continuous multi-site monitoring of pressure and temperature distribution for hemiplegic patient in wheelchair demonstrate the feasibility and stability of the strategically deployed sensor array for pressure relief using a support cushion and for lowering local pressures and skin temperatures using a water cushion. The other hemiplegic patient is a 56-year-old male with a height of 172 cm, a weight of 95.8 kg, blood pressure of 115/75 mmHg, albumin of 4.0 g dL^{-1}, and hemoglobin A1c (HbA1c) of 6.2%.

Figure 7a shows photographs of the patient sitting in wheelchair with addition of the support cushion or water cushion by a caregiver at a left sacrum, left ischium, and right heel. Figure 7b depicts IR photographs of the patient with addition of the water cushion with a temperature of about 18 °C, as shown in Figure 7b(i–iii). During the clinical trial, the caregiver sequentially placed the water cushion at the back, at the left ischium, and the right heel with 4 min intervals, as shown in Figures 7a(i–iii) and 7b(i–iii).

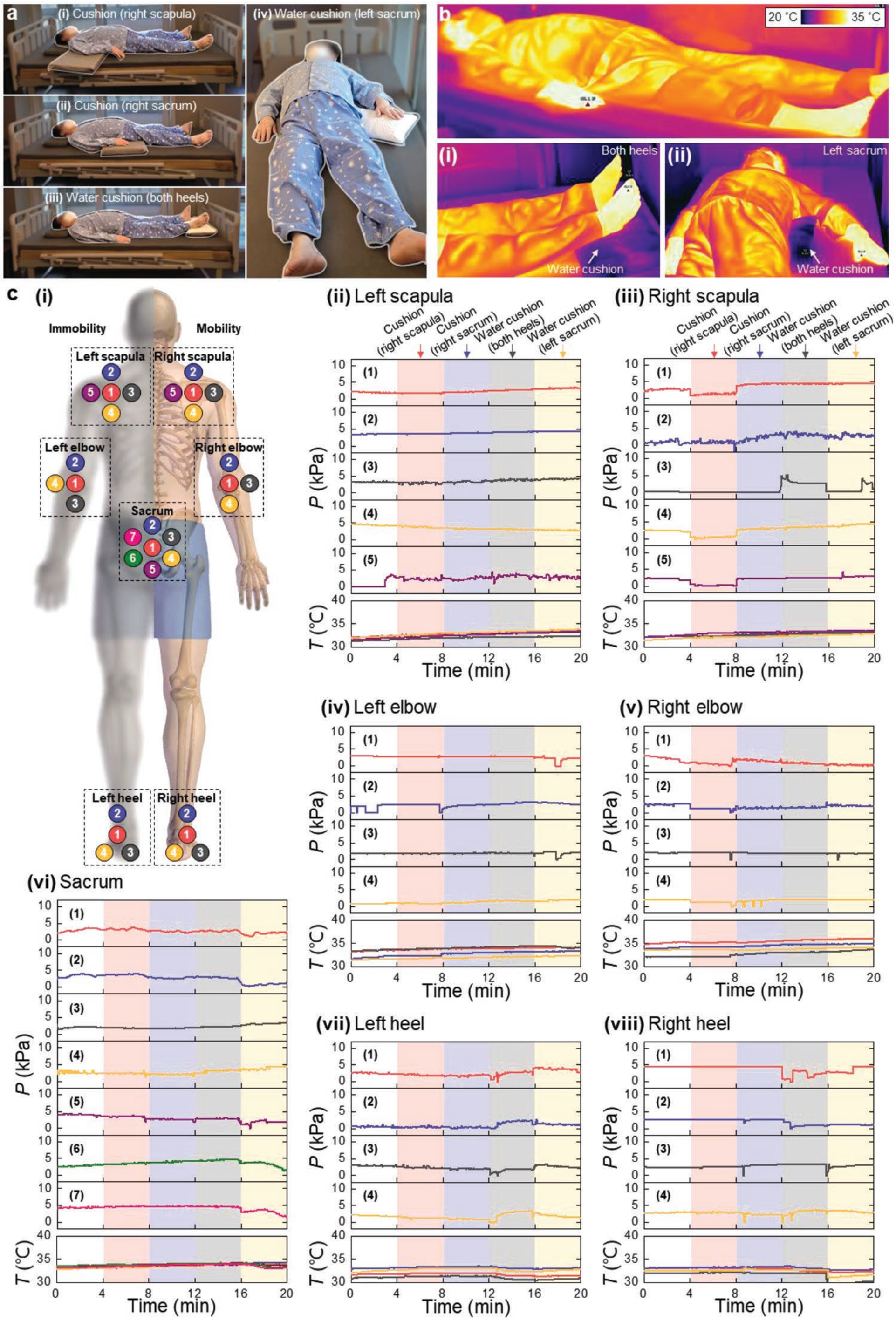

Figure 6. Continuous monitoring and mapping of pressure and temperature distribution at critical sites of a hospitalized, hemiplegic patient (62-year-old male, 73.9 kg, 162 cm) lying in clinical bed. a) Photographs of the patient lying in the clinical bed in a supine position for pressure relief based on the minimal repositioning of i) right scapula and ii) right sacrum using the support cushion and at iii) both heels and iv) left sacrum using the water cushion. b) IR images of the patient lying in the clinical bed with a water cushion under i) both heels and ii) left sacrum. c) i) Schematic anatomical diagram of 7 mounting locations of the sensor array. Results from continuous monitoring and mapping of pressure and temperature distribution from the sensor array mounted at ii,iii) both scapulae, iv,v) both elbows, vi) sacrum, and vii,viii) both heels.

Figure 7c(i) illustrates a schematic anatomical diagram of 5 mounting locations of the sensor array, including a sacrum, both ischia, and both heels of the left hemiplegic patient. Figure 7c(ii–vi) presents continuous multi-site recordings of temperature and pressure distribution measured from a hexagon-shaped array of 7 sensors at the sacrum, hexagon-shaped arrays of 7 sensors at both ischia, and pentagon-shaped arrays of 6 sensors at both heels.

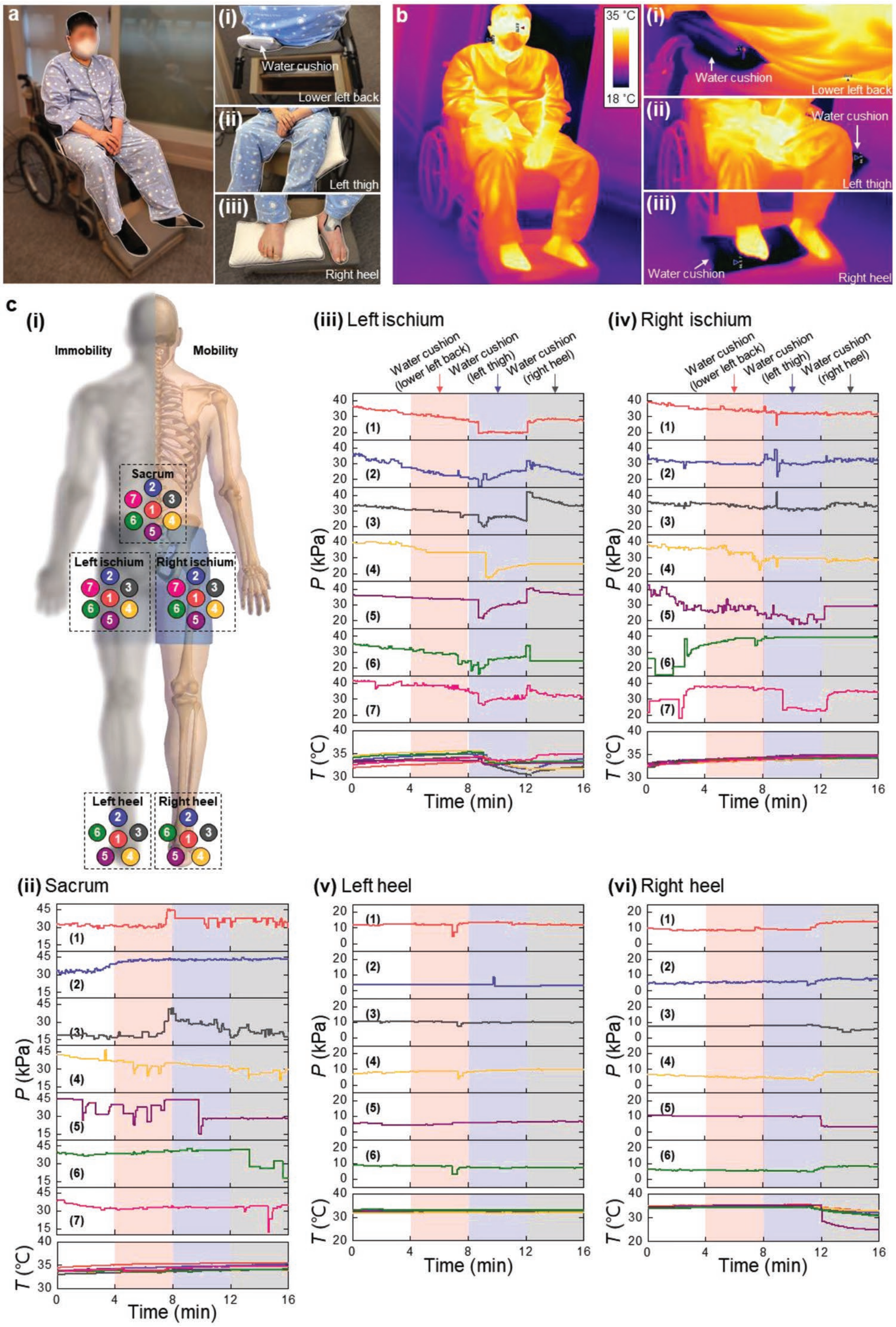

Figure 7. Continuous monitoring and mapping of pressure and temperature distribution at critical sites of a hospitalized, hemiplegic patient (56-year-old male, 95.8 kg, 172 cm) sitting in wheelchair. a) Photographs of the patient sitting in the wheelchair in a normal position for pressure relief based on the minimal repositioning at i) lower left back, ii) left ischium, and iii) right heel using the water cushion. b) IR images of the patient sitting in the wheelchair with addition of the water cushion placed at i) lower left back, ii) left ischium, and iii) right heel. c) i) Schematic anatomical diagram of 5 mounting locations of the sensor array. Results from continuous monitoring and mapping of pressure and temperature distribution from the sensor array mounted at ii) sacrum, iii,iv) both ischia, and v,vi) both heels.

Continuous multi-site monitoring of pressure and temperature distribution for a hemiplegic patient in a wheelchair demonstrates the feasibility and stability of the strategically deployed sensor array for pressure relief by a support cushion and for lowering local pressures and skin temperatures by a water cushion. Before explaining continuous monitoring data collected from the clinical trial in wheelchair, color maps that summarize the collected data along with a timeline that allows an intuitive understanding of the clinical trial in wheelchair at a glance in Figure S26, Supporting Information. Figure 7c(ii) presents a slight decrease in pressure at the sacrum (S4, S5) with increasing the pressure at the sacrum (S3) for 4 min by placing the water cushion at the lower left back, as shown in Figure 7a(i). Figure 7c(iii) depicts the pressure relief at the left ischium (S1, S3–S7) due to redistributing the weight to other parts by placing the water cushion at a left thigh. In Figure 7c(vi), the pressure value at the right heel fluctuated from placing the water cushion, indicating an increase in pressure (S1, S4, S6) and a decrease in pressure (S3, S5) at the right heel. Table S7, Supporting Information, shows the average values/ranges of temperature measured at the sacrum, both the ischia, and both the heels. Figure 7c(ii) shows a reduction in a local skin temperature at the left sacrum (S4–S7) and a maximum reduction of 0.6 °C at S7 for 4 min by placing the water cushion at interface between the left back and cushion. Figure 7c(iii) presents decrease in local skin temperature at the left ischium (S1–S7) by placing the water cushion at the interface between the left ischium. The local skin temperature at the left ischium (S3) decreased from 34.4 to 30.7 °C. Figure 7c(vi) presents a reduction in a local skin temperature at the right heel (S1–S6) by placing the water cushion at the interface between the right heel and footrest. In particular, a significant reduction in local skin temperature ranged from 35.6 to 25.3 °C occurs at S5 of the right heel. The maximum value of pressure at each location of interest is 46.5 kPa at the sacrum (S4), 42.1 kPa at the left ischium (S3), 43.0 kPa at the right ischium (S5), 14.0 kPa at the left heel (S1), and 14.5 kPa at the right heel (S1). Moreover, Video S3, Supporting Information, presents continuous multisite monitoring of pressure and temperature distribution from strategically deployed sensor arrays for a patient in a wheelchair through color maps. As previously reported, cooling of skin temperature up to 25 °C enable a reduction of the metabolic rate and the demand of nutrients in underlying tissues, which is one of strategical approaches to prevent pressure injuries.[39,40]

Figure S27, Supporting Information, compares PTI values between the single and multiple devices at each critical site for the patient in a wheelchair. The PTI values using the multiple devices show the average, maximum, and minimum values for each critical site at the same time. On the other hand, the PTI values obtained using a single device that depend on mounting locations show a lower value than the average at the left ischium and an average value at the sacrum, while they exhibit larger values than the average at the right ischium and both heels. These results indicate the PTI values using the multiple devices are useful for accurate risk assessment caused by sitting in a wheelchair.

3. Conclusion

This paper introduces a system capable of continuous multisite mapping of pressure and temperature distribution at critical locations prone to developing pressure injuries using strategically deployed sensor arrays of battery-free, wireless devices. In particular, the developed pressure sensor based on an internal flow of ionic liquid filled inside a pre-compressed microchannel provides excellent sensitivity as well as negligible hysteresis, high linearity, and cyclic stability over a relevant pressure range as required in these applications. In addition, the strategically deployed sensor array is useful to resolve a mismatch issue between the actual area of applied weight force and the effective area of the single sensor at critical skin interfaces. This approach supports the continuous monitoring of pressure and temperature distribution using the sensor arrays at different locations of a subject lying in clinical bed or sitting in wheelchair. Clinical trials on two hemiplegic patients demonstrated the feasibility of these sensor arrays across the whole body of subjects, which provides medical staffs with accurate, statistical information of pressure and temperature at locations of interest in real time. The collected data support the medical team to achieve cost effective pressure relief (e.g., minimal repositioning) in respect of labor force, time, and disease management without frequent repositioning or rolling the whole body of the subject, which leads to a high risk for back pain or musculoskeletal injuries.

This study focused on both normal pressure and temperature distribution that does not include the effect of additional ulcer-related variables, including shear, humidity, erythema and hemodynamics. Further advances in technologies for continuous monitoring and mapping of these additional variables could be helpful for the complete understanding and prevention of pressure injuries. In particular, smaller, thinner, more reliable pressure sensors could enable continuous monitoring of high-resolution pressure distribution along with a multiple ADC channels-assisted, battery-free, wireless sensing platform. In addition, defining algorithms and correlation between empirically collected data obtained in large-scale clinical trials and potential injuries of patients using machine learning analysis could provide thresholds for the early diagnosis of pressure injuries as a great potential for use in future precision healthcare.

4. Experimental Section

Fabrication of the Battery-Free, Wireless Platform: Fabrication began with patterning a sheet of flexible PCB substrate (fPCB; Pyralux AP 8535 R, DuPont, USA) using an ultraviolet laser cutter (ProtoLaser U4, LPKF Laser & Electronics AG, Germany). The electronic components, including NFC SoC (RF430FRL152H, Texas Instruments, USA), resistors (RC0201JR-07, Yageo, Taiwan) and capacitors (CL03B, Samsung Electro-Mechanics, South Korea) were mounted on the flexible PCB substrate using solder wire (SACX0307, Alpha Metal, USA) and solder paste (SMDLTLFP10T5, Chip Quick, Canada). An NFC SoC embedded with source codes stably supported power supplied from the primary antenna to the pressure sensor and temperature sensor. Digital signals converted from analog signals through internal ADCs with 14-bit resolution of the NFC SoC were transmitted to an NFC reader for wireless data communication according to the ISO 15693 protocol at 13.56 MHz. Low-loss tuning capacitors (GJM03-KIT-TTOL-DE, Murata Electronics, Japan) tuned the inductive reactance of the designed coil antenna at 13.56 MHz with a high-quality factor. One voltage divider that consisted of the pressure sensor and a tuning resistor converted fractional change in resistance of the pressure sensor to change in voltage of the ADC of NFC SoC. Likewise, the other voltage divider that included an NTC thermistor (NTCG064EF104FTBX, TDK Corporation, Japan) and a tuning resistor converted change in resistance of the NTC thermistor into change in voltage.

Fabrication of the Microfluidic Layer: Fabrication process began with spin coating (3000 rpm for 30 s) a negative photoresist (SU-8 2050, Kayaku Advanced Materials, Japan) on a silicon wafer followed by baking at 65 °C for 3 min and 95 °C for 6 min. Photolithography (UV irradiance of 170 mJ cm^{-2}) formed a master mold of SU-8 to define a microfluidic layer on the silicon wafer followed by baking the wafer at 65 °C for 1 min and 95 °C for 6 min. The master mold was immersed in a developer solution (SU-8 developer, Kayaku Advanced Materials, Japan) for 5 min 30 s, and then rinsed with isopropyl alcohol (IPA; J.T. Baker, USA) and distilled water. The master mold was treated with air plasma (CUTE, Femto Science, South Korea) at a power of 100 W for 10 min, and coated with trichloro(1*H*,1*H*,2*H*,2*H*-perfluorooctyl)silane (448931-10G, Sigma-Aldrich, USA) in vacuum overnight. Spin coating (400 rpm for 60 s) a mixture of polydimethylsiloxane (PDMS; Sylgard 184, Dow Inc., USA) and curing agent in a weight ratio of 10:1 on the master mold followed by baking at 70 °C for 4 h produces the microfluidic layer of PDMS.

Fabrication of the Ionic Liquid Pressure Sensor: The fabrication process began with bonding two Cu electrodes and a rigid substrate (glass wafer; $8 \times 8 \times 0.5$ mm^3) prepared with an ultraviolet laser system (ProtoLaser U4, LPKF Laser & Electronics AG, Germany) on the flexible PCB substrate using an epoxy resin (1365868-6, Loctite, USA). The two Cu electrodes was electrically connected to the designed flexible PCB circuit using silver epoxy (8331-14G, MG chemicals, Canada). A microfluidic layer (PDMS, $8 \times 8 \times 0.15$ mm^3) was treated using air plasma at a power of 100 W for 10 min, was immersed in a mixture solution of (3-mercaptopropyl)trimethoxysilane (MPTMS; 175 617, Sigma- Aldrich, USA) and methanol (J.T. Baker, USA) in a volume ratio (v/v) of 1:100,[41] and then was bonded on the rigid substrate using the epoxy resin. An ionic liquid (1-ethyl-3-methylimidazolium ethyl sulfate, Sigma- Aldrich, USA) was injected into the microfluidic layer using a syringe followed by sealing the inlet and outlet holes using the epoxy resin, as shown in Figure 1b,c and Figure S7c, Supporting Information. The ionic liquid was electrically connected to the two Cu electrodes. A soft block (PDMS; $1.0 \times 0.3 \times 0.4$ mm^3) was mounted on the center of microchannel in the microfluidic layer for pre-compression followed by sequentially incorporating a rigid frame defined by a rectangular shape with an opening in the middle (silicon wafer; $7 \times 7 \times 0.5$ and $8 \times 8 \times 0.5$ mm^3 inner and outer lateral dimensions) prepared by the UV laser system, a lower rigid pad (silicon wafer; $1.5 \times 1.5 \times 0.25$ mm^3), a polyimide membrane (PI; $8 \times 8 \times 0.075$ mm^3) with two cut openings (0.1×6 mm^2), and a upper rigid pad (silicon wafer; $3 \times 3 \times 0.5$ mm^3) using the epoxy resin (Figure S7f, Supporting Information). A soft frame defined a rectangular shape with an opening in the middle (PDMS; $7 \times 7 \times 0.5$ and $8 \times 8 \times 0.5$ mm^3 inner and outer lateral dimensions) with a width of 500 µm were cut by customized metallic punches, and then treated with MPTMS for enhancing an adhesion force to the PI membrane using the epoxy resin. Bonding a rigid cover (silicon; $8 \times 8 \times 0.25$ mm^3) on the soft frame and the upper rigid pad using the epoxy resin completes the ionic liquid pressure sensor ($8 \times 8 \times 2$ mm^3). The fabricated sensor was 8 mm wide and 1.95 mm thick (Figure S7h, Supporting Information).

Characterization of the Pressure and Temperature Sensors: A UTM (AGS-X, Shimadzu, Japan) with a source meter (Keithley 2400, Tektronix, Inc., USA) was used for evaluating characteristics of the pressure sensor. In addition, a micro actuator (MA-35, Physik Instrumente, Germany) and a load cell (SM S-type load cell, Interface, USA) were used for cyclic testing of the pressure sensor. Force data measured using the UTM was used to calculate the pressure, which enabled yielding a relationship between the pressure and fractional change in resistance collected from the source meter using a calibration process. For characterization of temperature sensor, an oven and hotplate were used in temperature range of 30 to 40 °C.

Finite Element Analysis (FEA): Abaqus commercial software (Dassault Systemes, France) was utilized to perform 2D FEA of the microchannel and 3D FEA of mechanics modeling of the devices: 1) roof deformation of microchannel in the microfluidic layer when applying the normal load at the soft block; and 2) corresponding strain distribution of the sensing platform under mechanical stimuli, including bending and twisting. The PMDS encapsulation (400 µm thick), PI (69 µm thick) and Cu layers (44 µm thick) were modeled by S4R shell element, and other components were modeled by C3D8R hexahedron element. The elastic modulus (E) and Poisson's ratio (υ) of the components for the analysis were $E_{\text{PDMS}} = 2.5$ MPa and $\upsilon_{\text{PDMS}} = 0.5$ for PDMS; $E_{\text{Glass}} = 50$ GPa and $\upsilon_{\text{Glass}} = 0.2$ for glass; $E_{\text{Si}} = 160$ GPa and $\upsilon_{\text{Si}} = 0.27$ for silicon; $E_{\text{PI}} = 2.5$ GPa and $\upsilon_{\text{PI}} = 0.34$ for polyimide; $E_{\text{Cu}} = 130$ GPa and $\upsilon_{\text{Cu}} = 0.34$ for copper.

NFC Protocols, Software, and Overall System: A RFID interface (TRF7970A Evaluation Module, Texas Instruments, USA) connected with a laptop computer provided the writing process in NFC SoC through a graphical user interface (GUI) according to ISO 15693 protocol at 13.56 MHz. The antenna reader (ID LRM2500, Feig Electronics, Germany) and ISOStart 2018 (Feig Electronics, Germany) supported the wireless data communication and power transfer between a primary antenna and a receiver antenna connected to NFC SoC. The primary antenna was set operated at a RF power of 8 W controlled by ISOStart 2018. The ADC values collected from the NFC SoC through the ISOStart 2018 were classified and visualized using Python software, which enables continuous, real-time monitoring of multiple devices. A system integrated with clinical bed included two primary antennas (ID ANT800/600, Feig Electronic, Germany), a multiplexer module (ID ANT.MUX.M4, Feig Electronic, Germany), the antenna reader, and a laptop computer as shown in Figure S20, Supporting Information. In addition, a system integrated with wheelchair included four primary antennas (antenna 1 and 2, ID ANT310/310, Feig Electronic, Germany; antenna 3 and 4, ID ANT200/200, Feig Electronic, Germany), the multiplexer module, the antenna reader, and a laptop computer in Figure 5a and Figure S22, Supporting Information.

Color Map of Pressure and Temperature: Contour plot for pressure and temperature distribution was created as follows: 1) points of mounting locations show measured values from each sensor; 2) midpoints of each mounting locations were calculated using linear interpolation with measured values from neighboring sensors; 3) outer area of sensor array represents the overall average of measured values; and 4) these values were displayed as color maps using data analysis software (OriginPro 8.5, OriginLab, USA).

Clinical Trials: An institutional review board (IRB) for clinical trials was approved from Pusan National University Hospital (institutional review board [IRB] number: 2111 017 109). Volunteers were recruited from population of the Kimhae Hansol Rehabilitation & Convalescent Hospital, and then signed consent forms for clinical trials. The volunteers included able-bodied subjects and two hemiplegic patients, but subjects who had pressure injuries were excluded based on medical records related to age, sex, height, weight, serum albumin level, hemoglobin A1c level, and severity of comorbidities. The clinical trials began with gently cleaning the locations of interest of the subject using alcohol wipes followed by attaching the sensor array using adhesive tapes. During the clinical trials, the skin temperature at the critical sites along with the water cushion was continuously captured using an infrared camera (Fortric 226, Fortric). After detaching the sensors, skin conditions on each critical location were evaluated by specialists.

Supporting Information

Supporting Information is available from the Wiley Online Library or from the author.

Acknowledgements

H.H. and Y.S.O. contributed equally to this work. H.H, and I.P. are supported by the Technology Innovation Program (00144157, Development of Heterogeneous Multi-Sensor Micro-System Platform) funded By the Ministry of Trade, Industry & Energy (MOTIE, korea). Y.S.O. is supported by Basic Science Research Program through the National Research Foundation of Korea (NRF) funded by the Ministry of Education (2020R1I1A1A0107489711). Z.X. acknowledges the support from the National Natural Science Foundation of China (Grant No. 12072057), LiaoNing Revitalization Talents Program (Grant No.

XLYC2007196), and the Fundamental Research Funds for the Central Universities (DUT22QN211). H.H., Y.S.O., and I.P. led the development of the concepts, designed the experiments, and interpreted results. H.H., Y.S.O., and I.P. wrote the paper.

Conflict of Interest

The authors declare no conflict of interest.

Data Availability Statement

All data needed to evaluate the conclusions in the paper are present in the paper and/or the Supplementary Materials. Additional data related to this paper may be requested from the corresponding authors.

Keywords

battery-free, ionic liquids, pressure injuries, pressure sensors, wireless

Received: August 17, 2022
Revised: October 20, 2022
Published online:

---

[1] Z. Li, F. Lin, L. Thalib, W. Chaboyer, *Int. J. Nurs. Stud.* **2020**, *105*, 103546.
[2] A. Kovindha, P. Kammuang-Lue, P. Prakongsai, T. Wongphan, *Spinal Cord* **2015**, *53*, 767.
[3] R. M. Allman, P. S. Goode, N. Burst, A. A. Bartolucci, D. R. Thomas, *Adv. Wound Care* **1999**, *12*, 22.
[4] N. Graves, F. Birrell, M. Whitby, *Infect. Control Hosp. Epidemiol.* **2005**, *26*, 293.
[5] H. Brem, J. Maggi, D. Nierman, L. Rolnitzky, D. Bell, R. Rennert, M. Golinko, A. Yan, C. Lyder, B. Vladeck, *Am. J. Surg.* **2010**, *200*, 473.
[6] J. Kottner, J. Cuddigan, K. Carville, K. Balzer, D. Berlowitz, S. Law, M. Litchford, P. Mitchell, Z. Moore, J. Pittman, D. Sigaudo-Roussel, C. Y. Yee, E. Haesler, *J. Tissue Viability* **2019**, *28*, 51.
[7] Y. S. Oh, J. H. Kim, Z. Xie, S. Cho, H. Han, S. W. Jeon, M. Park, M. Namkoong, R. Avila, Z. Song, S. U. Lee, K. Ko, J. Lee, J. S. Lee, W. G. Min, B. J. Lee, M. Choi, H. U. Chung, J. Kim, M. Han, J. Koo, Y. S. Choi, S. S. Kwak, S. B. Kim, J. Kim, J. Choi, C. M. Kang, J. U. Kim, K. Kwon, S. M. Won, et al., *Nat. Commun.* **2021**, *12*, 5008.
[8] S. Han, J. Kim, S. M. Won, Y. J. Ma, D. Kang, Z. Q. Xie, K. T. Lee, H. U. Chung, A. Banks, S. Min, S. Y. Heo, C. R. Davies, J. W. Lee, C. H. Lee, B. H. Kim, K. Li, Y. D. Zhou, C. Wei, X. Feng, Y. G. Huang, J. A. Rogers, *Sci. Transl. Med.* **2018**, *10*, eaan4950.
[9] J. W. Kwak, M. Han, Z. Xie, H. U. Chung, J. Y. Lee, R. Avila, J. Yohay, X. Chen, C. Liang, M. Patel, I. Jung, J. Kim, M. Namkoong, K. Kwon, X. Guo, C. Ogle, D. Grande, D. Ryu, D. H. Kim, S. Madhvapathy, C. Liu, D. S. Yang, Y. Park, R. Caldwell, A. Banks, S. Xu, Y. Huang, S. Fatone, J. A. Rogers, Wireless Sensors for Continuous, Multimodal Measurements at the Skin Interface with Lower Limb Prostheses **2020**.
[10] Y. Park, K. Kwon, S. S. Kwak, D. S. Yang, J. W. Kwak, H. Luan, T. S. Chung, K. S. Chun, J. U. Kim, H. Jang, H. Ryu, H. Jeong, S. M. Won, Y. J. Kang, M. Zhang, D. Pontes, B. R. Kampmeier, S. H. Seo, J. Zhao, I. Jung, Y. Huang, S. Xu, J. A. Rogers, *Sci. Adv.* **2020**, *6*, eabe1655.
[11] J. Kim, M. Lee, H. J. Shim, R. Ghaffari, H. R. Cho, D. Son, Y. H. Jung, M. Soh, C. Choi, S. Jung, K. Chu, D. Jeon, S. T. Lee, J. H. Kim, S. H. Choi, T. Hyeon, D. H. Kim, *Nat. Commun.* **2014**, *5*, 5747.
[12] B. Nie, R. Huang, T. Yao, Y. Zhang, Y. Miao, C. Liu, J. Liu, X. Chen, *Adv. Funct. Mater.* **2019**, *29*, 1808786.
[13] J. Ahmad, H. Andersson, J. Sidén, *IEEE Sens. J.* **2019**, *19*, 2055.
[14] P. Zhu, Y. Wang, Y. Wang, H. Mao, Q. Zhang, Y. Deng, *Adv. Energy Mater.* **2020**, *10*, 2001945.
[15] B. U. Hwang, A. Zabeeb, T. Q. Trung, L. Wen, J. D. Lee, Y. I. Choi, H. B. Lee, J. H. Kim, J. G. Han, N. E. Lee, *NPG Asia Mater.* **2019**, *11*, 23.
[16] S. Kim, M. Amjadi, T. I. Lee, Y. Jeong, D. Kwon, M. S. Kim, K. Kim, T. S. Kim, Y. S. Oh, I. Park, *ACS Appl. Mater. Interfaces* **2019**, *11*, 23639.
[17] K. Kim, J. Choi, Y. Jeong, I. Cho, M. Kim, S. Kim, Y. Oh, I. Park, *Adv. Healthcare Mater.* **2019**, *8*, 1900978.
[18] Y. Kim, A. Chortos, W. Xu, Y. Liu, J. Y. Oh, D. Son, J. Kang, A. M. Foudeh, C. Zhu, Y. Lee, S. Niu, J. Liu, R. Pfattner, Z. Bao, T. W. Lee, *Science* **2018**, *360*, 998.
[19] J. Choi, D. Kwon, K. Kim, J. Park, D. Del Orbe, J. Gu, J. Ahn, I. Cho, Y. Jeong, Y. Oh, I. Park, *ACS Appl. Mater. Interfaces* **2020**, *12*, 1698.
[20] K. H. Ha, W. Zhang, H. Jang, S. Kang, L. Wang, P. Tan, H. Hwang, N. Lu, *Adv. Mater.* **2021**, *33*, 2103320.
[21] D. Kwon, T. I. Lee, J. Shim, S. Ryu, M. S. Kim, S. Kim, T. S. Kim, I. Park, *ACS Appl. Mater. Interfaces* **2016**, *8*, 16922.
[22] L. Yuan, Z. Wang, H. Li, Y. Huang, S. Wang, X. Gong, Z. Tan, Y. Hu, X. Chen, J. Li, H. Lin, L. Li, W. Hu, *Adv. Mater. Technol.* **2020**, *5*, 1901084.
[23] Z. Chen, Z. Wang, X. Li, Y. Lin, N. Luo, M. Long, N. Zhao, J. B. Xu, *ACS Nano* **2017**, *11*, 4507.
[24] K. Y. Lee, H. J. Yoon, T. Jiang, X. Wen, W. Seung, S. W. Kim, Z. L. Wang, *Adv. Energy Mater.* **2016**, *6*, 1502566.
[25] F. R. Fan, L. Lin, G. Zhu, W. Wu, R. Zhang, Z. L. Wang, *Nano Lett.* **2012**, *12*, 3109.
[26] N. Bergstrom, B. Braden, *J. Am. Geriatr. Soc.* **1992**, *40*, 747.
[27] J. Y. Kokate, K. J. Leland, A. M. Held, G. L. Hansen, G. L. Kveen, B. A. Johnson, M. S. Wilke, E. M. Sparrow, P. A. Iaizzo, *Arch. Phys. Med. Rehabil.* **1995**, *76*, 666.
[28] P. A. Iaizzo, *Wounds* **2004**, *16*, 336.
[29] J. Kim, A. Banks, H. Cheng, Z. Xie, S. Xu, K. I. Jang, J. W. Lee, Z. Liu, P. Gutruf, X. Huang, P. Wei, F. Liu, K. Li, M. Dalal, R. Ghaffari, X. Feng, Y. Huang, S. Gupta, U. Paik, J. A. Rogers, *Small* **2015**, *11*, 906.
[30] C. J. Boyle, D. Carpanen, T. Pandelani, C. A. Higgins, M. A. Masen, S. D. Masouros, *PLoS One* **2020**, *15*, e0227064.
[31] M. Hubli, R. Zemp, U. Albisser, F. Camenzind, O. Leonova, A. Curt, W. R. Taylor, *Spinal Cord* **2021**, *59*, 175.
[32] J. Leys, M. Wübbenhorst, C. P. Menon, R. Rajesh, J. Thoen, C. Glorieux, P. Nockemann, B. Thijs, K. Binnemans, S. Longuemart, *J. Chem. Phys.* **2008**, *128*, 064509.
[33] W. L. Yuan, X. Yang, L. He, Y. Xue, S. Qin, G. H. Tao, *Front. Chem.* **2018**, *6*, 59.
[34] W. Sae-Sia, D. D. Wipke-Tevis, D. A. Williams, *Appl. Nurs. Res.* **2005**, *18*, 29.
[35] W. Sae-Sia, D. D. Wipke-Tevis, D. A. Williams, *Arch. Phys. Med. Rehabil.* **2007**, *88*, 1673.
[36] M. Ishihara, K. Fujiki, K. Umetani, E. Hiraki, in *2019 IEEE Energy Convers. Congr. Expo. ECCE 2019*, IEEE, Piscataway, NJ **2019**, p. 4584.
[37] H. U. Chung, B. H. Kim, J. Y. Lee, J. Lee, Z. Xie, E. M. Ibler, K. H. Lee, A. Banks, J. Y. Jeong, J. Kim, C. Ogle, D. Grande, Y. Yu, H. Jang, P. Assem, D. Ryu, J. W. Kwak, M. Namkoong, J. Bin Park, Y. Lee, D. H. Kim, A. Ryu, J. Jeong, K. You, B. Ji, Z. Liu, Q. Huo, X. Feng, Y. Deng, Y. Xu, et al., *Science* **2019**, *363*, eaau0780.
[38] M. A. Serghiou, J. Niszczak, I. Parry, R. Richard, *Burns* **2016**, *42*, 267.
[39] Y. T. Tzen, D. M. Brienza, P. Karg, P. Loughlin, *J. Tissue Viability* **2010**, *19*, 86.
[40] Y. T. Tzen, D. M. Brienza, P. E. Karg, P. J. Loughlin, *J. Spinal Cord Med.* **2013**, *36*, 357.
[41] M. V. Hoang, H. J. Chung, A. L. Elias, *J. Micromech. Microeng.* **2016**, *26*, 105019.